



HAL
open science

The Day the Solar Wind Disappeared at Mars

J. S. Halekas, S. Shaver, A. R. Azari, C. M. Fowler, Y. Ma, S. Xu, L. Andersson, C. Bertucci, S. M. Curry, C. Dong, et al.

► **To cite this version:**

J. S. Halekas, S. Shaver, A. R. Azari, C. M. Fowler, Y. Ma, et al.. The Day the Solar Wind Disappeared at Mars. *Journal of Geophysical Research Space Physics*, 2023, 128, 10.1029/2023JA031935 . insu-04473118

HAL Id: insu-04473118

<https://insu.hal.science/insu-04473118>

Submitted on 22 Feb 2024

HAL is a multi-disciplinary open access archive for the deposit and dissemination of scientific research documents, whether they are published or not. The documents may come from teaching and research institutions in France or abroad, or from public or private research centers.

L'archive ouverte pluridisciplinaire **HAL**, est destinée au dépôt et à la diffusion de documents scientifiques de niveau recherche, publiés ou non, émanant des établissements d'enseignement et de recherche français ou étrangers, des laboratoires publics ou privés.



Distributed under a Creative Commons Attribution - NonCommercial - ShareAlike 4.0 International License

JGR Space Physics



RESEARCH ARTICLE

10.1029/2023JA031935

Key Points:

- An extremely low-density solar wind stream encountered the Earth and Mars just after Mars opposition in December 2022
- The Martian magnetosheath developed very unusual properties, with a low level of plasma instabilities and a high ion anisotropy
- The Martian magnetosphere and its boundaries expanded by thousands of km, extending outside of the location of the nominal bow shock

Supporting Information:

Supporting Information may be found in the online version of this article.

Correspondence to:

J. S. Halekas,
jasper-halekas@uiowa.edu

Citation:

Halekas, J. S., Shaver, S., Azari, A. R., Fowler, C. M., Ma, Y., Xu, S., et al. (2023). The day the solar wind disappeared at Mars. *Journal of Geophysical Research: Space Physics*, 128, e2023JA031935. <https://doi.org/10.1029/2023JA031935>

Received 27 JUL 2023
Accepted 19 OCT 2023

Author Contributions:

Conceptualization: J. S. Halekas, S. Shaver, A. R. Azari

Data curation: J. S. Halekas, L. Andersson, T. Hara, J. P. McFadden, D. L. Mitchell









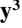






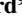

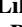






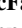

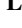



Formal analysis: J. S. Halekas, S. Shaver, A. R. Azari, C. M. Fowler, Y. Ma, S. Xu

Investigation: J. S. Halekas, S. Shaver, A. R. Azari, C. M. Fowler, Y. Ma, S. Xu

Methodology: J. S. Halekas, S. Shaver, A. R. Azari, C. M. Fowler, Y. Ma, S. Xu

Resources: J. S. Halekas

The Day the Solar Wind Disappeared at Mars

J. S. Halekas¹ , S. Shaver² , A. R. Azari³ , C. M. Fowler⁴ , Y. Ma⁵ , S. Xu³ , L. Andersson² , C. Bertucci⁶ , S. M. Curry³ , C. Dong⁷ , Y. Dong² , X. Fang² , P. Garnier⁸ , K. G. Hanley³ , T. Hara³ , S. K. Howard^{9,10} , A. Hughes⁹ , R. J. Lillis³ , C. O. Lee³ , J. G. Luhmann³ , H. Madanian² , M. Marquette³ , C. Mazelle⁸ , J. P. McFadden³ , K. Meziane¹¹ , D. L. Mitchell³ , A. Rahmati³ , W. Reed² , N. Romanelli^{9,12} , and N. R. Schnepf² 

¹Department of Physics and Astronomy, University of Iowa, Iowa City, IA, USA, ²Laboratory for Atmospheric and Space Physics, University of Colorado, Boulder, CO, USA, ³Space Sciences Laboratory, University of California Berkeley, Berkeley, CA, USA, ⁴Department of Physics and Astronomy, West Virginia University, Morgantown, WV, USA, ⁵Department of Earth, Planetary and Space Sciences, UCLA, Los Angeles, CA, USA, ⁶IAFE, UBA-CONICET, Buenos Aires, Argentina, ⁷Department of Astronomy, Boston University, Boston, MA, USA, ⁸IRAP, CNES, CNRS, UPS, Université de Toulouse, Toulouse, France, ⁹NASA Goddard Space Flight Center, Greenbelt, MD, USA, ¹⁰Department of Physics and Astronomy, Howard University, Washington, DC, USA, ¹¹Physics Department, University of New Brunswick, Fredericton, NB, Canada, ¹²Department of Astronomy, University of Maryland, College Park, MD, USA

Abstract In December 2022, an extremely low-density solar wind stream encountered first the Earth and then Mars, shortly after the radial alignment of the two planets (i.e., Mars opposition). As the low-density stream passed Mars, the properties of the Mars-solar wind interaction changed dramatically in response to the low solar wind Alfvénic Mach number and dynamic pressure. The Martian magnetosphere and its boundaries expanded by thousands of kilometers, extending outside of the nominal average bow shock location. The low upstream Mach number resulted in a low ratio of plasma to magnetic field pressure in the magnetosheath, allowing the formation of a very high but stable ion temperature anisotropy, together with a very low level of electromagnetic instabilities. Meanwhile, the decrease in solar wind dynamic pressure caused the Martian upper ionosphere at the terminator to transition from a magnetized state to an unmagnetized state. This event provides an opportunity to study a unique end-member state of the Mars-solar wind interaction.

Plain Language Summary The solar wind consists of a supersonic flow of hot ionized gas (plasma) from the Sun that flows outward through the solar system. The solar wind interacts with planetary atmospheres and magnetic fields, which form shielded regions known as magnetospheres. The characteristics of the solar wind, including its density and speed, vary over a wide range. The shape, extent, and physical characteristics of planetary magnetospheres in turn respond to these changes in the solar wind. In this work, we study the response of the Martian magnetosphere to an extremely low-density solar wind stream. During the passage of this stream, the Martian magnetosphere expanded by thousands of kilometers, and its physical characteristics changed dramatically. This event reveals a unique outlier state for the Mars-solar wind interaction.

1. Introduction

Mars has a unique interaction with the ambient space plasma environment, thanks to the combination of its atmosphere, exosphere, and remanent crustal magnetic fields (Acuña et al., 1998; Bertucci et al., 2011; Dubinin et al., 2006; Mazelle et al., 2004; Nagy et al., 2004). These elements of the Martian obstacle together produce a unique “hybrid” interaction with the solar wind and interplanetary magnetic field (IMF), not entirely like either the intrinsic magnetosphere of Earth or the more purely induced magnetosphere of Venus, but with aspects of both (Brain et al., 2003; DiBraccio et al., 2018; Dubinin et al., 2023; Halekas et al., 2021).

Planetary magnetospheres facilitate the interactions between planets and the impinging solar wind, controlling the flow of energy and momentum through the system. The properties of these magnetospheres (e.g., intrinsic, induced, or hybrid) determine which physical processes dominate in diverting the solar wind flow around the obstacle, and control how efficiently the solar wind can couple to the planet and deposit energy into the system. The Martian magnetosphere (including the upper atmosphere and ionosphere) and its boundaries react to a variety of internal and external drivers, including solar wind and IMF conditions, seasonal and other changes in the upper atmosphere and exosphere, and the orientation of the planet (and thus the location of the crustal magnetic fields). The bow shock (BS) size and shape have been shown to respond to changes in the solar

© 2023. The Authors.

This is an open access article under the terms of the [Creative Commons Attribution-NonCommercial-NoDerivs](https://creativecommons.org/licenses/by/4.0/) License, which permits use and distribution in any medium, provided the original work is properly cited, the use is non-commercial and no modifications or adaptations are made.

Software: J. S. Halekas, S. Shaver, A. R. Azari, C. M. Fowler, Y. Ma, S. Xu, L. Andersson, T. Hara, K. Meziane, D. L. Mitchell

Supervision: J. S. Halekas

Validation: J. S. Halekas, S. Shaver, A. R. Azari, C. M. Fowler, Y. Ma, S. Xu, L. Andersson, C. Bertucci, S. M. Curry, C. Dong, Y. Dong, X. Fang, P. Garnier, K. G. Hanley, T. Hara, S. K. Howard, A. Hughes, R. J. Lillis, C. O. Lee, J. G. Luhmann, H. Madanian, M. Marquette, C. Mazelle, J. P. McFadden, K. Meziane, D. L. Mitchell, A. Rahmati

Writing – original draft: J. S. Halekas, S. Shaver, A. R. Azari, C. M. Fowler

Writing – review & editing: J. S. Halekas, S. Shaver, A. R. Azari, C. M. Fowler, Y. Ma, S. Xu, L. Andersson, C. Bertucci, S. M. Curry, C. Dong, Y. Dong, X. Fang, P. Garnier, K. G. Hanley, T. Hara, S. K. Howard, A. Hughes, R. J. Lillis, C. O. Lee, J. G. Luhmann, H. Madanian, M. Marquette, C. Mazelle, J. P. McFadden, K. Meziane, D. L. Mitchell, A. Rahmati, W. Reed

wind dynamic pressure, Mach number, IMF direction, extreme ultraviolet (EUV) flux, and the orientation of the crustal magnetic fields (Edberg et al., 2008, 2009, 2010; Garnier et al., 2022; Gruesbeck et al., 2018; Halekas, Ruhunusiri, et al., 2017; Hall et al., 2019; Sui et al., 2023; Trotignon et al., 2006; Verigin et al., 1993; Vignes et al., 2002; Wang et al., 2020). The magnetospheric boundaries, such as the nearly co-located induced magnetosphere boundary (IMB), magnetic pileup boundary (MPB), ion composition boundary (ICB), and photoelectron boundary (PEB), also shift in response to external and internal factors (Edberg et al., 2008; Garnier et al., 2017; Halekas et al., 2018; Holmberg et al., 2019; Matsunaga et al., 2017; Trotignon et al., 2006; Vignes et al., 2000; Xu et al., 2016, 2023). Furthermore, the force balance and the morphology of the flows and fields in the magnetosheath and magnetosphere react to many of the same drivers (Halekas, Brain, et al., 2017).

At the Earth and Venus, periods of abnormally low solar wind density result in substantial increases in the spatial extent (i.e., standoff distance) of the BS and the magnetospheric boundaries (Cairns et al., 1995; Fairfield, 1971; Hajra & Tsurutani, 2022; Russell & Zhang, 1992; Steinolfson & Cable, 1993; Tatrallyay et al., 1983; Wei et al., 2012; T. L. Zhang et al., 2008). One particularly dramatic case observed at the Earth was dubbed “The Day the Solar Wind Disappeared” (Fairfield et al., 2001; Janardhan, 2006; Janardhan et al., 2008; Lazarus, 2000). At Mars, such events remain comparatively less studied, though examples do exist in the literature (Verigin et al., 2004).

The Martian atmosphere and ionosphere play a particularly important role in the Mars-solar wind interaction. Appreciable fluxes of planetary ions are observed at the interaction boundary, in the magnetosheath, in the magnetotail, and even in the near-Mars upstream solar wind, where they can affect the pressure balance and the kinetic state of the plasma. “Space weather” events such as coronal mass ejections and flares, as well as solar wind structures such as stream interaction regions, introduce extremes of external conditions that produce Martian magnetospheric disturbances far different from Earth's geomagnetic storms (Jakosky et al., 2015; Luhmann et al., 2017). Periods of low solar wind density represent a distinctive solar wind transient that has received less attention as both a solar/heliospheric phenomenon and as a driver of the Mars-solar wind interaction. Given the above considerations, we expect that low-density events may have implications for escape of planetary ions from Mars.

Periods of low solar wind density typically result in smaller values of the dynamic pressure $P_{dyn} = \rho_{sw} v_{sw}^2$ (with ρ_{sw} and v_{sw} the solar wind mass density and speed) and the Alfvén and magnetosonic Mach numbers $M_A = v_{sw}/v_A$ and $M_{MS} = v_{sw}/v_{MS}$ (with $v_A = B/\sqrt{\mu_0 \rho}$ and $v_{MS} = \sqrt{c_s^2 + v_A^2}$ the solar wind Alfvén and magnetosonic speeds). These changes in the solar wind in turn lead to expansion and changes in the shape of the BS and the magnetospheric boundaries. Furthermore, since β (the ratio of thermal pressure $nk_B T$ to magnetic pressure $B^2/2\mu_0$) in the magnetosheath scales with upstream M_A , low Mach numbers affect the growth and evolution of β -dependent plasma instabilities in the magnetosheath (Gary et al., 1993; Halekas, Brain, et al., 2017; Hill et al., 1995). This may have particularly interesting effects at Mars, which has a relatively small magnetosheath thickness in terms of relevant ion scales, leaving little room for solar wind ions to fully thermalize (Brecht, 1997; Moses et al., 1988). The unique hybrid Martian magnetosphere may therefore react to unusual solar wind conditions in different ways than a more purely intrinsic or induced magnetosphere such as those of the Earth and Venus.

In this manuscript, we describe a recent “disappearing solar wind” event observed by the Mars Atmosphere and Volatile Evolution (MAVEN) spacecraft (Jakosky et al., 2015) in December 2022 at Mars. We discuss the upstream conditions and the response of the magnetosheath and the magnetosphere of Mars in the following sections. The purpose of this paper is to provide a general overview of the characteristics of this event and to identify aspects of the event deserving of more detailed analysis in future studies.

2. The Upstream Conditions

On 2022 December 25 an extended region of very low-density solar plasma ($0.1\text{--}0.2\text{ cm}^{-3}$) passed the Earth. Roughly a day later, on December 26, a similar structure passed Mars. Fortunately, this event took place just a few weeks after Earth-Mars opposition on December 08, so Earth and Mars encountered very similar plasma structures, as shown in Figure 1. We utilize measurements made by the MAVEN Solar Wind Ion Analyzer (SWIA, Halekas et al. (2015)) and Magnetometer (MAG, Connerney et al. (2015)) to characterize the region upstream from the Martian BS, as well as the magnetosheath and magnetosphere. We utilize Mars-Solar-Orbital (MSO) coordinates, defined with $+x$ toward the Sun, $+z$ northward and normal to the orbital plane, and $+y$ completing the right-handed coordinate system. To specifically identify the upstream region and isolate the incident solar wind and IMF parameters, we utilize the algorithms described in Halekas, Ruhunusiri, et al. (2017).

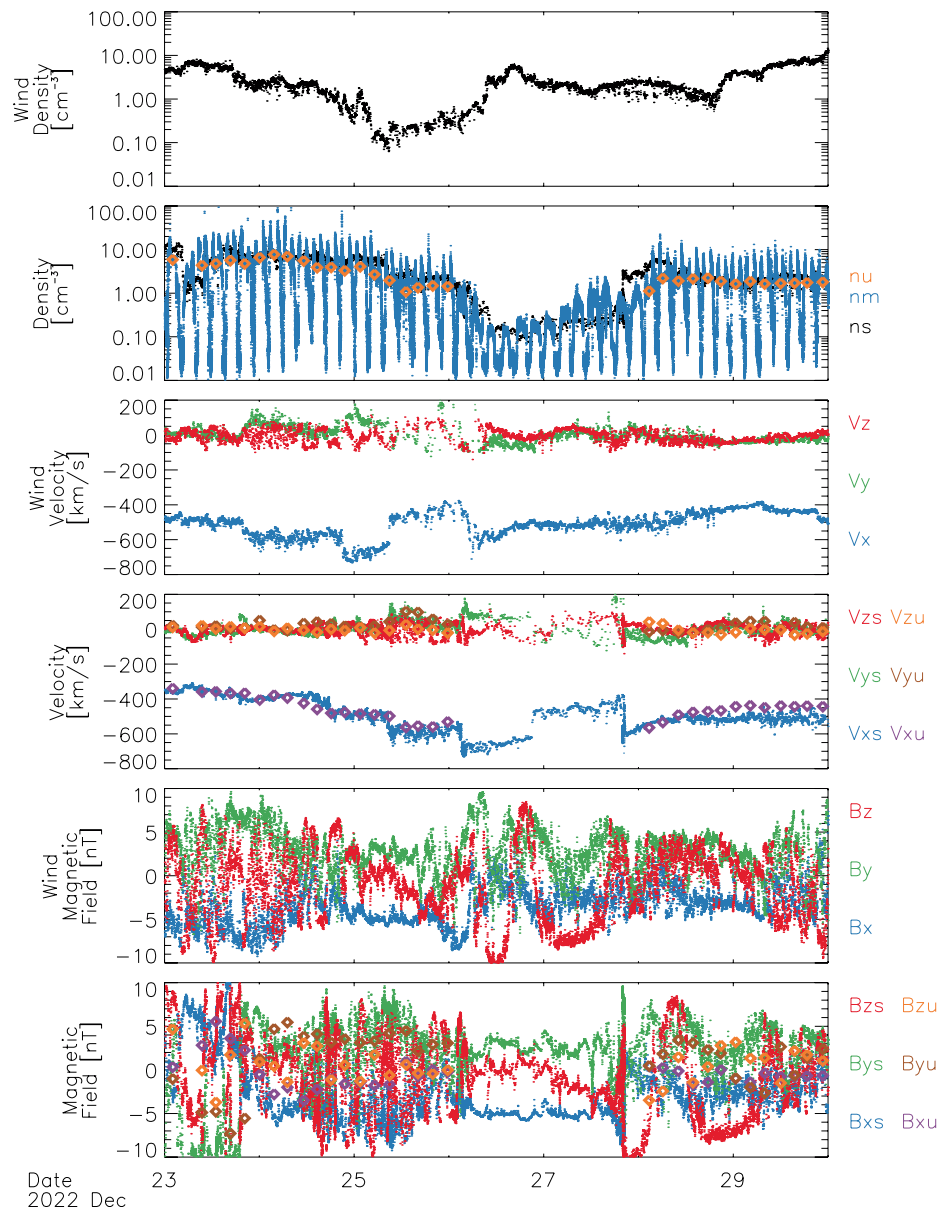


Figure 1. Solar wind and interplanetary magnetic field (IMF) observations near Mars and Earth. The first, third, and fifth panels show solar wind density (n), velocity (V), and IMF (B) measured by Wind at the Earth-Sun L1 point. The second, fourth, and sixth panels show orbit-average solar wind and IMF values measured by MAVEN (colored diamonds, nu , Vu , Bu) upstream from the Martian bow shock (BS), compared to time-shifted Wind observations (colored dots, ns , Vs , Bs , with propagation delays calculated as described in text). Panel 2 also shows instantaneous densities measured by MAVEN (blue dots, nm) inside the BS, in addition to those in the upstream region. Vector quantities measured by Wind utilize Geocentric-Solar-Ecliptic (GSE) coordinates and those measured by MAVEN utilize Mars-Solar-Orbital (MSO) coordinates; these coordinate systems are aligned to within 10 degrees at this time.

During the deepest portion of the density minimum, the Martian BS expanded to such a degree that MAVEN did not directly sample the upstream solar wind for over a day. To characterize the upstream solar wind, and for comparative purposes, we therefore also show measurements made by the Wind spacecraft near the Earth-Sun L1 Lagrange point (well upstream of the region of terrestrial influence, even during these unusual conditions). Specifically, we utilize ion data from the Solar Wind Experiment (SWE, Ogilvie et al. (1995)) and magnetic field data from the Magnetic Field Investigation (MFI, Lepping et al. (1995)) to characterize the solar wind and IMF near Earth.

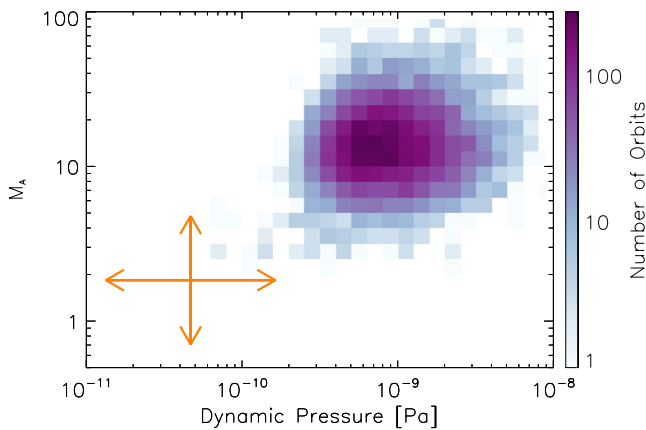


Figure 2. Distribution of solar wind dynamic pressure and Alfvén Mach number measured by MAVEN in the undisturbed solar wind upstream from the Martian bow shock from 2014 November to 2023 February (one average upstream value per orbit). Orange arrows show the range of minimum and maximum values for dynamic pressure and Mach number, for the low-density period on 26–27 December 2022 estimated from L1 and MAVEN data as described in text.

To compare the observations from Earth and Mars more directly, we time-shift the Wind observations to approximately account for propagation delays. We first ballistically map the Wind observations radially outward, utilizing the solar wind speed measured near the Earth (i.e., we calculate $\Delta t = \Delta R/V_{sw}$ as a function of time). We boxcar smooth the resulting time increments to eliminate non-physical outcomes such as faster solar wind parcels passing through slower solar wind parcels. Since Earth and Mars do not line up exactly radially during this time period (though nearly so), they do not experience exactly the same structures launched from the same location on the Sun at the same time. To best align the Earth and Mars observations, we reduce the Δt calculated above by an empirically estimated constant offset of 8 hr. This offset accounts for the fact that the Earth leads Mars by $\sim 9^\circ$ in rotational phase during this time period, and we therefore observe a combination of radial propagation and co-rotation of structures. We do not scale the Wind observations in any way; however, we do expect lower magnitudes of both density and magnetic field at Mars due to the expansion of the wind.

We find that the time-shifted Wind observations correspond quite well with the MAVEN upstream observations. The solar wind velocity matches very closely in magnitude, and even has similar off-axis components. As expected, the solar wind density at Mars appears generally reduced from that observed at Earth, but not always to the $\sim 40\%$ of the Earth value one would predict for

an r^{-2} reduction between the radial locations of the two planets at this time. Both the MAVEN and Wind measurements have been calibrated to absolute standards (i.e., the plasma frequency), so the smaller than expected reduction in density likely represents a real physical effect; however, the mechanisms remain unclear. In any case, the MAVEN and time-shifted Wind observations of the plasma density and velocity have very similar temporal behavior, suggesting that the time-shifting procedure we adopted captures the propagation of the large-scale structures from Earth to Mars, at least to first order. On the other hand, the magnetic fields correlate somewhat less well than the plasma parameters. Before the low-density period, the Wind and MAVEN magnetic field measurements match fairly well, with quite similar features, and roughly the expected reduction in magnitude from Earth to Mars. The IMF orientation generally appears less radial at Mars than at Earth, consistent with the larger expected Parker spiral angle at Mars. After the low-density period, however, the magnetic field observed at Mars differs more significantly from that at Earth in both polarity and magnitude. This suggests a more complex evolution of the fields in these structures, possibly resulting from the interaction between the faster stream trailing the slower stream at the end of the low-density period.

To estimate the solar wind parameters during the density minimum, we utilize the parameters measured by Wind, with a range of scaling assumptions between the expected radial scaling and the observed scaling before/after the event. We assume that the solar wind density lies between the values observed at 1 AU and 50% of those values, a range of $0.05\text{--}0.2\text{ cm}^{-3}$. We assume that the solar wind speed lies within the range observed by Wind, 400–700 km/s. We assume that the magnetic field magnitude lies between the values observed at 1 AU and 60% of those values, a range of 3–5.8 nT. Given this conservatively broad range of values, we infer that the upstream dynamic pressure at Mars during the density minimum most likely lies in the range $P_{dyn} \sim 1.34 \times 10^{-11} - 1.64 \times 10^{-10}$ Pa, and that the Alfvén Mach number most likely lies in the range $M_A \sim 0.7 - 4.8$. Even the upper ends of these ranges lie far from the typical solar wind parameters at Mars, $P_{dyn} \sim 5 \times 10^{-10} - 10^{-9}$ Pa and $M_A \sim 10 - 20$.

We next evaluate how these fundamental solar wind parameters compare to the range of solar wind conditions typically encountered at Mars. In Figure 2, we compare the estimated low-density event parameters to the frequency distribution of the same parameters computed from the upstream solar wind values observed by MAVEN from 2014 November to 2023 February, derived from MAG and SWIA observations using the algorithm described in Halekas, Ruhunusiri, et al. (2017).

We find that, even if the dynamic pressure and Mach number for the 2022 December event lie at the upper ends of the ranges inferred from time-shifted Wind measurements, they still represent extreme outliers in the distribution of solar wind parameters observed by MAVEN. MAVEN upstream observations include no more than a few other orbits with comparable conditions over the entire mission. We note that extremely low-density events

such as this one will not necessarily be represented in the upstream parameter data set, since the BS can expand well outside of the apoapsis of the MAVEN orbit under these conditions, making direct solar wind measurements impossible. Regardless, this event represents a unique opportunity to investigate the Mars-solar wind interaction under end-member solar wind conditions.

3. The Magnetosheath

In the terrestrial magnetosphere, low- M_A solar wind flows lead to a number of unusual conditions, including the development of asymmetries in the magnetospheric boundaries and flows, and changes in the operation of magnetic reconnection and instabilities (Lavraud & Borovsky, 2008). In addition, the ion temperature anisotropy T_{\perp}/T_{\parallel} in the magnetosheath increases at low M_A (Dimmock et al., 2015), particularly downstream of the quasi-perpendicular shock (Soucek et al., 2015). This high ion temperature anisotropy results in large part from the low β that prevails in the magnetosheath during low- M_A conditions. Passage through the BS naturally heats solar wind ions in the perpendicular direction, by a factor of as much as $\sim 10 - 20$ (Sckopke et al., 1983, 1990; Thomsen et al., 1985). For high- β conditions, the thresholds for perpendicular anisotropy-driven instabilities such as mirror mode and kinetic Alfvén-ion cyclotron waves remain low, and plasma instabilities act to reduce the ion anisotropies and bring the ion distributions closer to isotropy (Gary et al., 1993, 1994; Hill et al., 1995; Sckopke et al., 1990; Soucek et al., 2015). In low- β conditions, on the other hand, larger ion anisotropies can persist without triggering instabilities. Similar considerations apply at Mars, and statistical studies using MAVEN observations have confirmed that higher average ion temperature anisotropies occur in the Martian magnetosheath under low- M_A conditions downstream of the quasi-perpendicular BS (Halekas, Brain, et al., 2017).

In Figure 3, we compare ion and magnetic field observations made by MAVEN before and during the low-density period. In the pre-event orbit, MAVEN encounters the magnetosheath from 04:05-04:20 and from 05:57-06:45 UT, and the solar wind during the intervening time period. In the low-density orbit, MAVEN encounters the magnetosheath from 09:45-11:30 UT, and does not directly sample the solar wind. During both orbits, one can infer a comparable IMF orientation, given the $+B_y, -B_x$ orientation observed in the magnetosheath (also consistent with the IMF orientation seen in the solar wind on the pre-event orbit). Therefore, we expect that the significant differences in the observed magnetosheath characteristics on the two orbits result mainly from the very different plasma parameters, rather than geometric effects. Given that MAVEN's apoapsis lies in the $+Y$ hemisphere at this time, this nominally places it downstream from the quasiperpendicular BS for the magnetosheath portion of both orbits.

The vector magnetic field and ion spectra during the low-density orbit appear much more smooth and laminar than in the pre-event orbit, with few fluctuations apparent. In order to characterize the level of magnetic field fluctuations as a function of frequency, we compute a wavelet transform of the vector magnetic field, utilizing a Morlet wavelet. We find a lower level of fluctuations by an order of magnitude or more in the magnetosheath at all frequencies during the low-density orbit, and an almost complete lack of magnetic field fluctuations at frequencies above the proton cyclotron frequency $\Omega_{cp} \sim 0.2 \text{ s}^{-1}$.

Moments computed by direct integration over the measured ion distribution have high inaccuracies during the low-density time period, due to the combination of low signal to noise and high ion anisotropy. We therefore estimate the ion temperature components by fitting the SWIA 3-d coarse distributions (Halekas, Ruhunusiri, et al., 2017) to the convecting bi-Maxwellian distribution function

$$f(v_{\perp}, v_{\parallel}) = n \left(\frac{m}{2\pi k_B} \right)^{3/2} \frac{1}{T_{\perp}} \frac{1}{\sqrt{T_{\parallel}}} \exp \left[-\frac{m}{2k_B} \left(\frac{(v_{\perp 1} - v_{b1})^2}{T_{\perp}} + \frac{(v_{\perp 2} - v_{b2})^2}{T_{\perp}} + \frac{(v_{\parallel} - v_{b3})^2}{T_{\parallel}} \right) \right] \quad (1)$$

where n is the bulk density, v_{\parallel} is the ion velocity component parallel to the magnetic field, $v_{\perp 1}$ and $v_{\perp 2}$ are the two velocity components perpendicular to the magnetic field, v_{bi} are the bulk velocity components, and T_{\perp} and T_{\parallel} are the temperature components perpendicular and parallel to the magnetic field. We utilize a least squares fitting method with a gradient descent algorithm to retrieve the fit parameters, incorporating an additional fit parameter to account for the instrumental background due to galactic cosmic rays and natural radioactivity in the microchannel plate detectors (constant count rate over energy). See Figure S1 in Supporting Information S1 for an example of these fits. The lower angular and energy resolution of the coarse SWIA data we utilize for this fitting procedure limits our ability to resolve very low temperatures, so we consider the results only an upper limit in the solar wind, and more appropriate for the hotter ion distributions of the magnetosheath.

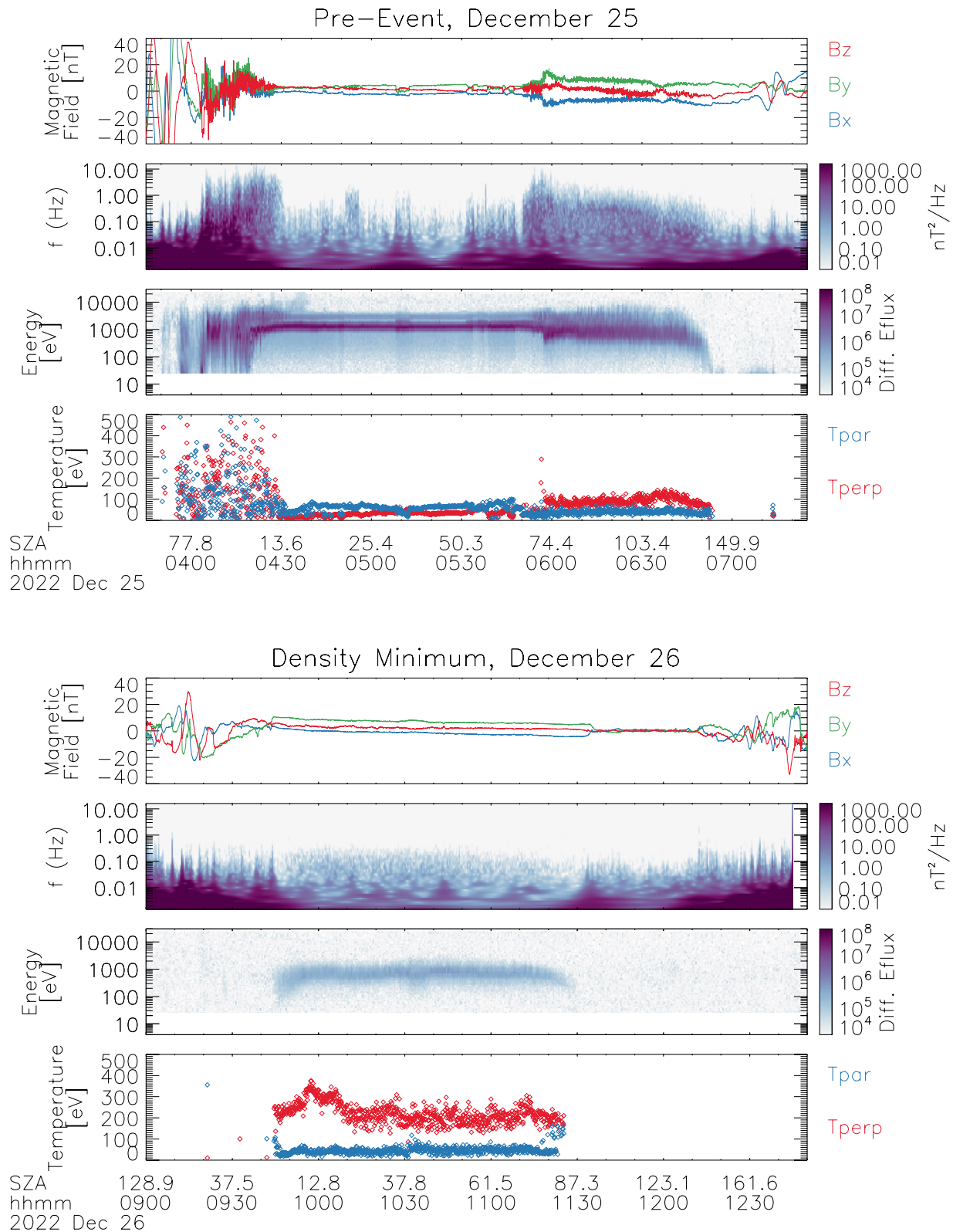


Figure 3. Comparison of MAVEN time series observations for one pre-event orbit (top four panels) and one orbit during the low-density event (bottom four panels), with each orbit starting at periaapsis, outbound to apoapsis, then inbound to periaapsis. Panels show magnetic field vector components (MSO coordinates), wavelet spectra of magnetic field fluctuations, ion differential energy flux [eV/(cm² s sr eV)], and ion temperatures parallel and perpendicular to the magnetic field, derived from the fitting procedure described in text.

The results from this fitting procedure reveal a very high ion anisotropy during the low-density event, peaking at $T_{\perp}/T_{\parallel} \sim 8$ in the sub-solar region of the magnetosheath, consistent with the large compression ratio and quasi-perpendicular geometry expected there for the observed IMF conditions. The perpendicular temperature reaches 200–300 eV, an order of magnitude larger than the typical solar wind temperature, consistent with the expected heating at the quasi-perpendicular BS. During the pre-event orbit, on the other hand, we find comparable temperatures in the outbound magnetosheath (closer to the subsolar point, and coincident with high levels of magnetic field fluctuations), but only minor departures from isotropy. In the solar wind, we interpret the fit results as an upper limit, particularly for T_{\parallel} , since the presence of the alpha particles erroneously increases this value (Halekas, Ruhunusiri, et al., 2017). Finally, in the inbound magnetosheath (closer to the flank), we find a much lower temperature and moderate anisotropies, but none that exceed ~ 2.5 (other than a few points right at the shock). The combination of significant total heating and high anisotropy in the magnetosheath during the low-density event appears completely unlike the conditions observed in either the outbound or inbound magnetosheath on the pre-event orbit.

During the low density time period, multiple orbits occurred that would under nominal conditions pass through the BS. The high ion anisotropy observed suggests that the solar wind has interacted with a BS, which indicates that the BS has expanded past the orbit of MAVEN to an altitude $>4,500$ km (MAVEN's apoapsis during this period). In contrast, the nominal maximum extent of the BS lies closer to $\sim 2,000$ km altitude on the day side (Gruesbeck et al., 2018).

The juxtaposition of low levels of magnetic fluctuations and very high ion anisotropies observed in the magnetosheath during the low-density event is unusual and interesting. The very low level of instabilities suggests at least marginal stability of the ion distributions. We find a proton $\beta_p \sim 0.1 - 0.3$ in the magnetosheath at this time, with a very low $\beta_{lp} \leq 0.05$. This would imply anisotropy thresholds for the proton cyclotron instability of $T_{\perp}/T_{\parallel} \sim 3$ (Gary et al., 1994), smaller than what we observe. However, we note that ion distributions with anisotropies higher than the proton cyclotron threshold do occur at these low β_{lp} values in the solar wind (Hellinger & Mangeney, 1999). If the ion distributions observed by MAVEN are in fact stable, this may suggest that the ion temperatures we observe during the low-density event provide a relatively unmodified view of the heating due to the passage of the ions through the shock. With comparisons to theoretical models and/or simulations, this could allow one to make inferences about the nature of the shock during these unique solar wind conditions. In any case, the low level of instabilities observed by MAVEN suggests that these highly anisotropic conditions likely prevail throughout the magnetosheath, as they do in the portion that MAVEN accesses. This may also result in alterations from the typical field and flow patterns in the magnetosheath, as well as a somewhat unusual balance of forces at the MPB and ICB. These rare conditions could also alter the Martian magnetosphere.

4. The Magnetosphere

As the solar wind approaches Mars, the incoming IMF geometry is distorted, due to a combination of mass loading and draping around the conductive obstacle formed by Mars' ionosphere. This interaction results from the presence of the Martian hybrid magnetosphere, which at high altitudes strongly resembles the induced magnetospheric interaction at Venus (e.g., Cloutier et al., 1999; Law & Cloutier, 1995; Luhmann, 1986; Luhmann & Russell, 1997; McComas et al., 1986). Recent findings have extended this theoretical picture to the now extensive observations of MAVEN, by showing that the full three dimensional IMF geometry, particularly the radial (X in MSO) component affects the dayside draping in predictable ways, when considering Mars as an induced obstacle (Azari et al., 2023). Further studies have shown the global repercussions of Mars' planetary ion plume, which perturbs this basic picture and alters the draped field line morphology (Chai et al., 2019; C. Zhang et al., 2022).

However, at low altitudes (particularly under 800 km), the Mars interaction differs markedly from that in typical induced magnetospheres, due to the presence of remanent crustal magnetic fields that alter the draping morphology, from the day side to the tail (Azari et al., 2023; DiBraccio et al., 2018, 2022). This leads to a strong altitude dependence in magnetic field geometry over the day side, as a result of the interplay of the IMF, the induced magnetic field, and the crustal fields. Under nominal conditions, this creates a dynamic system in which magnetic field draping depends on the upstream IMF geometry and the observer location in both MSO (to capture the induced/solar wind interaction) and areographic coordinates (to capture the crustal field interaction).

Under the low density conditions of this event, we would expect this nominal draping picture to differ. As previously mentioned, during this period of low solar wind density, MAVEN does not encounter the BS for almost

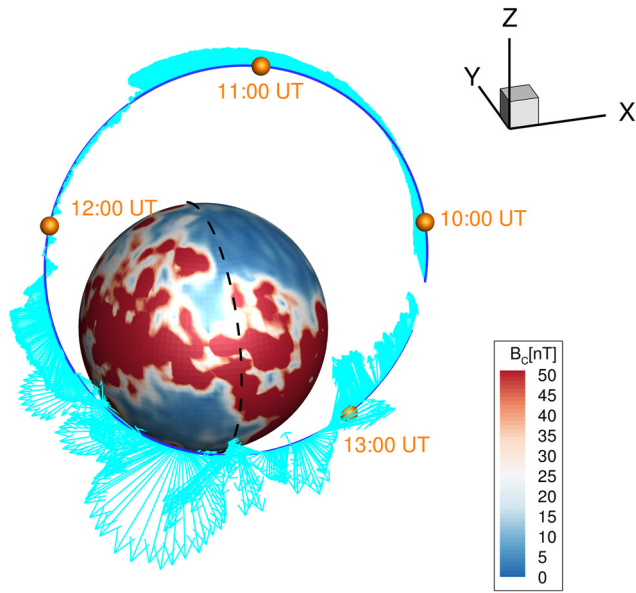


Figure 4. Three-dimensional magnetic field configuration over one MAVEN orbit during the low-density minimum, on 26 December 2022 (same orbit as Figure 3, bottom panels). The cyan whiskers along the orbit depict the direction and magnitude of the measured magnetic field in MSO coordinates. Periapsis occurs above the night side of the planet, where the spacecraft passes through strong crustal fields. Orange points on the orbit indicate the UT time of each observation. Mars is represented by a sphere, with the model crustal field magnitude from Morschhauser et al. (2014) overlaid in color. The black dashed line on the sphere indicates the terminator location, with the day side to the right.

a day, between December 26 at 10:00 and December 28 at 02:00 UT. The observed expansion of the BS suggests that the magnetic field draping over the day side should also effectively increase in altitude in comparison to nominal conditions. The observations from MAVEN and at L1 (see Figure 1) suggest that the IMF geometry also changes over this low density period, as the IMF direction before and after the event ($+B_y$, $-B_x$ vs. $+B_z$ respectively) differs.

Figure 4 shows the magnetic field observed by MAVEN, in MSO coordinates, during the minimum solar wind density period on December 26. At 10:00 UT, in the magnetosheath region, the magnetic field configuration generally follows a draped configuration, lying mainly in the $+Y$ and $-X$ MSO direction, which aligns with the most recent observation of the solar wind. However, near $\sim 11:30$ UT, the magnetic field decreases dramatically in magnitude and changes direction. The very low magnetic field strength continues until the spacecraft encounters strong crustal magnetic fields after 12:00 UT, which dominate the measured magnetic field near periapsis. The region of near-zero magnetic field will be discussed further below.

Changes in the upstream solar wind conditions like those during this low-density solar wind event can impact the Mars-solar wind interaction and the physical processes that control it. The transition region from shocked solar wind to ionospheric plasma in the Martian magnetosphere contains multiple boundary layers, with disparate definitions that depend historically on the specific instruments available on specific spacecraft. Below the magnetosheath, the transition regions observed by MAVEN include the ICB, the IMB, and the PEB. These boundaries can consist of sharp transitions; however, they often extend over a range of altitudes, forming boundary layers (Holmberg et al., 2019). The locations of these boundary layers, and the characteristics of the plasma above and below the boundaries, offer insight into the structure and extent of the Martian ionosphere and magnetosphere.

The IMB (Bertucci et al., 2011; Dubinin et al., 2006; Lundin et al., 2004) represents a transition below which suprathermal electrons with energies higher than 100 eV are no longer observed and magnetic field fluctuations decrease. A rotation in the magnetic field is often observed across the boundary. The IMB represents a transition from shocked solar wind plasma to ionospheric plasma. The IMB typically lies at an altitude between 650 and 800 km above the Martian day side (Holmberg et al., 2019; Matsunaga et al., 2017). We manually identify the IMB in this study by using SWEA (Mitchell et al., 2016) observations to determine where electrons with energies near 100 eV dissipate and MAG (Connerney et al., 2015) measurements to locate a coincident rotation in the magnetic field.

The ICB (Breus et al., 1991; Halekas et al., 2018; Sauer et al., 1994) represents the transition from light ion species of solar wind origin at higher altitudes to heavy ionospheric species at lower altitudes. The ICB typically lies at 600–650 km; however, it sometimes coincides with the IMB or even lies above it in altitude (Holmberg et al., 2019; Xu et al., 2016). In this study, we utilize ion measurements from STATIC (McFadden et al., 2015) to locate this boundary, by determining where the ion composition transitions from light ion (H^+ and He^+) dominated to heavy ion (O^+ and O_2^+) dominated.

The PEB (Dubinin et al., 2006; Garnier et al., 2017; Mitchell et al., 2001; Xu et al., 2023) represents a topological boundary that separates magnetic field lines having access to the dayside ionosphere (open or closed) and primarily populated by ionospheric photoelectrons from those connected to the solar wind on both ends (draped) and populated by electrons of solar wind origin. The PEB on average lies at approximately the same altitude as the ICB and within the ICB transition region (Xu et al., 2023). In this study, we utilize photoelectron energy and pitch angle distributions to locate the PEB, using the methodology described in Xu et al. (2023). We use a shape parameter less than 0.7 to define the highest altitude location of the PEB in closed-to-day, cross-terminator, and open-to-day directions. We utilize the more strict 0.7 threshold (compared to the more typical value of 1), because we observe photoelectrons originating from flux tubes of differing origins.

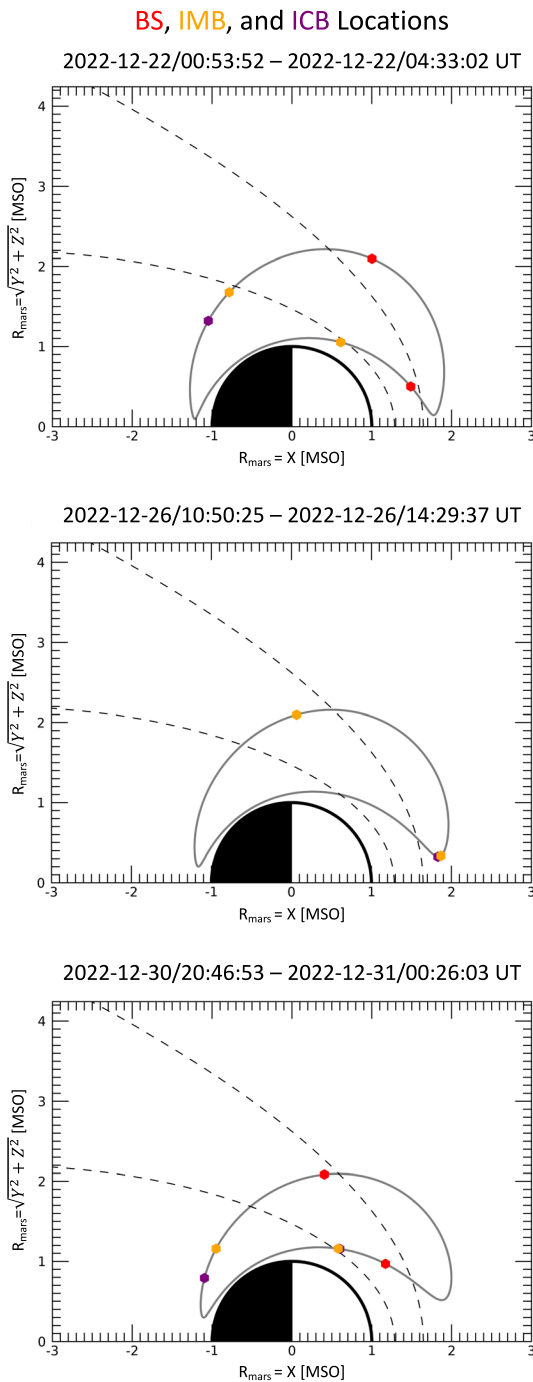


Figure 5. Locations of the bow shock (BS, red points), induced magnetosphere boundary (IMB, orange points), and ion composition boundary (ICB, purple points) for three orbits, in MSO coordinates. From top to bottom, the orbits shown by the gray solid line occur before, during, and after the low-density solar wind period. During the low-density event, MAVEN does not observe the BS, so the center panel contains no red points. Black dashed lines indicate the nominal location of the BS and magnetic pileup boundary (Vignes et al., 2000). The MAVEN orbit follows a counterclockwise trajectory in each panel.

Figure 5 shows three single orbits of MAVEN, on December 22 before the low-density event, on December 26 during the solar wind density minimum (partially overlapping with the time interval of Figures 3 and 4), and on December 30 after the event. Colored points indicate the location of the BS, IMB, and ICB along each of these orbits. See Figures S2–S4 in Supporting Information S1 for particle and magnetic field data utilized to determine these locations. Note that the ICB and IMB are co-located on the outbound portion of December 22 and the inbound portion of December 26. Meanwhile, Figure 6 depicts all locations of the IMB, ICB, and PEB during the time interval from December 22 through December 30. During the solar wind density minimum, the three magnetospheric boundaries all reach altitudes outside of the nominal average BS location in the subsolar region. At higher solar zenith angles (SZA), the boundaries exhibit large differences in their observed location both before and after the two orbits with the minimum solar wind density.

During the pre-event orbits, the IMB, ICB, and PEB all lie close to the nominal MPB conic shape (Vignes et al., 2000) in both the subsolar (outbound) and flank (inbound) regions. On December 26, during the solar wind density minimum, the subsolar location (SZA $\sim 10^\circ$) of the three boundaries expands from an altitude of ~ 500 km up to $\sim 3,000$ km over the course of about two days before returning to pre-event altitudes one day later. On the inbound orbit segments, at higher SZA, the three boundaries reach altitudes greater than 3,500 km during the low-density event. After the event, from December 26 at 04:00 UT to December 27 at 06:00 UT, the observed altitude of the IMB becomes highly variable, moving from a maximum altitude of 3,760 km at 26 December 2022/15:09:30 to a minimum altitude of 1,392 km at 26 December 2022/19:31:10. A separate study will discuss these boundary locations in detail and compare to statistical distributions over the MAVEN mission.

The observed locations of the Martian magnetospheric boundaries (Figures 5 and 6) demonstrate the greatly expanded state of the ionosphere and magnetosphere during the low-density period. To complement this analysis, we also investigate the pressure balance across the boundary region (Figure 7). Typically, the Martian ionosphere remains in a magnetized state, implying that above the day side the solar wind dynamic pressure exceeds the ionospheric plasma pressure, allowing the solar wind IMF to penetrate into the ionosphere. The magnetic field strength typically reaches a few tens of nanotesla within the magnetized ionosphere in regions without strong crustal magnetic fields. Prior to the minimum in solar wind density, and in particular, during the orbit immediately prior to this minimum, MAVEN observed magnetic field strengths of 2–7 nT within the upper ionosphere. However, during the inbound segment of the orbit immediately following the minimum in solar wind density, the spacecraft encountered a greatly expanded upper ionosphere at the dusk terminator north of the equator. Coincident with encountering the low energy thermal plasma of the upper ionosphere, the magnetic field strength dropped from 7 nT in the magnetosheath to consistently < 1 nT within the upper ionosphere (see Figure 4). The lower ionosphere does not change significantly during this time period, so this alteration in the upper ionosphere does not appear to reflect effects from lower altitudes.

Figure 7 shows the various pressure terms calculated from MAVEN observations as the spacecraft encounters the expanded tenuous upper ionosphere, immediately following the minimum in solar wind density. Prior to 11:20, MAVEN lies within the magnetosheath, which has almost equal plasma and magnetic pressures (brown and black lines) during this time period. As

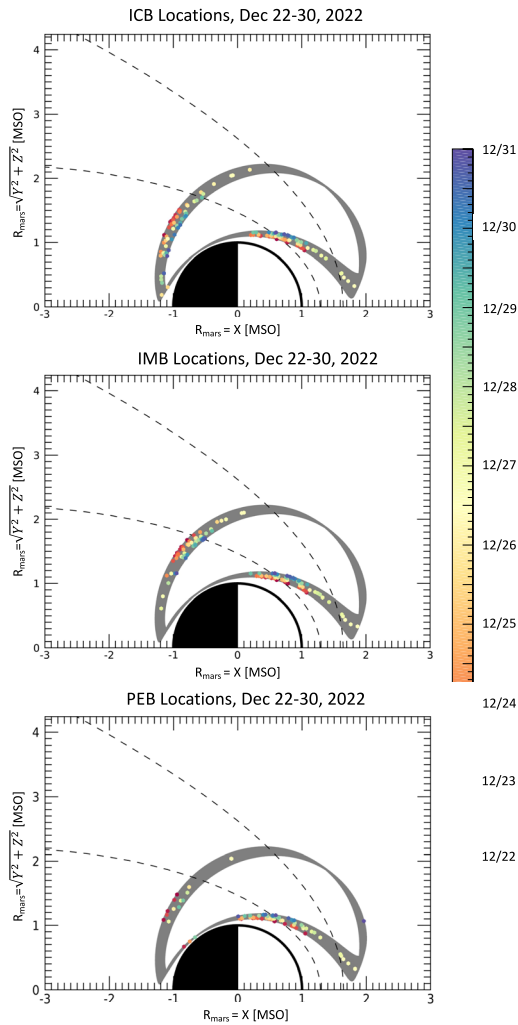


Figure 6. From top to bottom: Locations of the ion composition boundary, induced magnetosphere boundary, and PEB in MSO coordinates for all orbits during the 2022 December 22–31 time period, with color indicating the time of the boundary crossing. Gray solid lines show MAVEN orbit segments. Black dashed lines indicate the nominal location of the bow shock and magnetic pileup boundary (Vignes et al., 2000). The MAVEN orbit follows a counterclockwise trajectory in each panel.

MAVEN exits the magnetosheath and enters a boundary region, the plasma pressure (brown line) drops and the magnetic pressure dominates. The drop in plasma pressure in this boundary region is not fully understood. MAVEN then encounters the tenuous upper ionosphere at 11:35. Here, the magnetic pressure drops by over two orders of magnitude, and the suprathermal and thermal electron plasma pressures (green and purple lines) increase significantly and dominate. The measured ion thermal pressure (blue line) remains 1–2 orders smaller than the electron pressures, due to field of view limitations that prevent STATIC from observing the full ion distribution. Pressure balance holds across the transition into the upper ionosphere, suggesting that the ionospheric plasma pressure is strong enough to stand off the solar wind dynamic pressure at the terminator upper ionosphere and prevent the IMF from penetrating into the ionosphere, explaining the consistently low (<1 nT) magnetic field strength there. The near-terminator Mars solar wind-ionosphere interaction thus changes from a magnetized to an unmagnetized state during the solar wind density minimum. These pressure balance observations will be discussed in more detail in a separate study.

MAVEN crosses the sun-shadow boundary at 12:07 UT. Here, the spacecraft potential jumps by several volts, and we note discontinuities in the plasma observations. These artificial discontinuities will be analyzed in a separate paper, which also discusses a variety of instrumental effects that arise due to MAVEN encountering the expanded upper ionosphere at such high altitudes, and operating in modes optimized to observe high energy plasma rather than cold ionospheric plasma. Later in the orbit, after 12:20, MAVEN encounters stronger crustal magnetic fields (orange line). The upper ionosphere remains in an expanded and unmagnetized state for two orbits during the solar wind density minimum, before returning to a magnetized state as the solar wind density and dynamic pressure recover to pre-event values.

5. Conclusions and Implications

The event described in this manuscript represents an extreme outlier for the Mars-solar wind interaction. A detailed study of the solar source(s) of this event is currently in progress. Regardless of the solar origin, the solar wind dynamic pressure and Alfvén Mach number M_A both reach low values very seldom observed at Mars. Moreover, this combination of solar wind parameters likely can only occur in the inner solar system. The solar wind Mach number generally increases with heliocentric distance, while the dynamic pressure falls rapidly. Thus, only in the inner solar system would we expect to encounter this combination of conditions for a solar wind-planetary interaction. While many of the moons of the giant planets also experience low- M_A flows, they are typically immersed in hotter sub-magnetosonic plasma, often composed of heavier ions, resulting in a rather different interaction. There-

fore, the conditions achieved in this event may prove unique to the inner planets (at least within our solar system). Given the unusual hybrid Mars-solar wind interaction, the MAVEN observations discussed herein therefore represent a one of a kind opportunity to study a unique physical interaction.

While this manuscript provides a general overview of the event and its characteristics, numerous aspects of the observations still deserve further study, through both data analysis and simulation approaches. Modern magnetohydrodynamic and hybrid simulations will play an important role in providing context for the spacecraft observations and establishing the global interaction. Data from other spacecraft should be incorporated in the analysis (e.g., Mars Express made relevant observations during this time period, and other spacecraft such as Tianwen-1 may have also returned relevant data). In addition, the current observations should be placed in context with other similar events, as well as compared and contrasted with observations obtained under other unusual

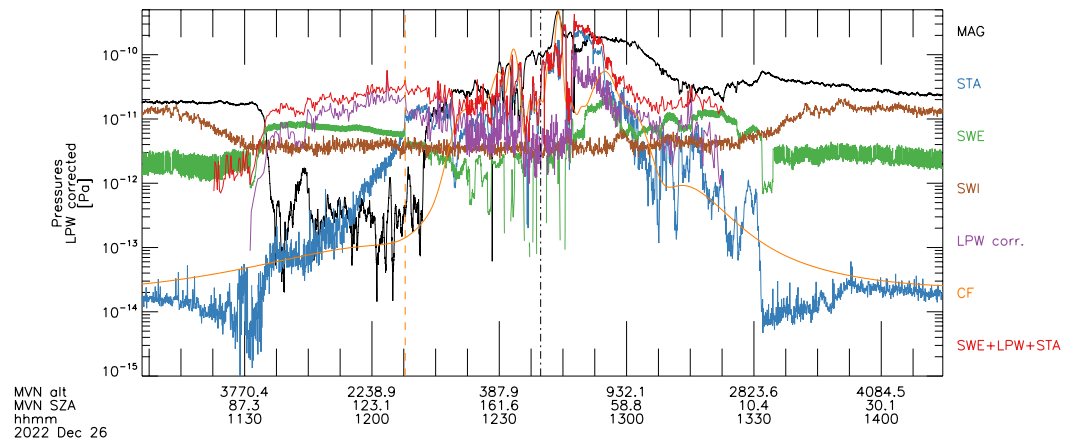


Figure 7. Pressure terms calculated from MAVEN observations for the inbound orbit segment immediately following the solar wind density minimum (same time interval as the middle panel of Figure 5). MAG = magnetic pressure calculated via $B^2/2\mu_0$; STA, SWE, SWI and LPW = plasma pressures calculated from STATIC, SWEA, SWIA, and LPW data via $n_s k_B T_s$, where subscript s denotes ions or electrons; CF = magnetic pressure from the crustal field model of Morschhauser et al. (2014); SWE + LPW + STA shows total ionospheric thermal plasma pressure. The vertical orange and black dashed lines indicate the sun-shadow boundary and the periapsis locations. Note: We derive LPW thermal electron density and temperature using empirical methods to mitigate instrumental effects. SWIA pressure becomes constant just after 11:30 at a value of $\sim 3.6 \times 10^{-12}$ Pa; this represents the instrument background level due to penetrating cosmic rays and detector background.

solar wind conditions. The positions and shapes of the BS and magnetospheric boundaries should be more quantitatively compared with the distribution of average and extreme locations previously observed. The magnetic field draping morphology, and the interplay between temporal changes and expansion of the boundaries, should be carefully analyzed. The escape of ions from Mars and the relative importance of different escape processes during these unique conditions should be investigated. The kinetic microstate of the plasma and the electrodynamic environment at all scales should also be more thoroughly characterized.

Finally, we envision several speculative possibilities potentially also worthy of investigation. The unusual magnetospheric morphology and the high ion anisotropies may affect the details of the pressure balance throughout the interaction region. The extreme expansion of the ionosphere may affect the magnetic morphology and topology, or it might lead to a more purely induced and Venus-like interaction, at least above some regions of the planet. The extremely low density of the solar wind permits the existence of non-Maxwellian solar wind ion and electron distributions with significant non-thermal populations; their presence may in turn affect the Mars interaction. We hope that this manuscript provides a starting point for those interested in conducting such investigations, as well as others that we have not yet identified.

Data Availability Statement

The research described in this manuscript utilizes publicly available data from the MAVEN mission, including data from the SWIA, SWEA, MAG, and STATIC instruments (Connerney, 2017; Halekas, 2017; Mcfadden, 2023; Mitchell, 2017). We also utilized data from the Wind SWE and MFI instruments (Koval et al., 2021; Ogilvie et al., 2021) for context. All data were processed using the publicly available SPEDAS software (Angelopoulos et al., 2019).

References

- Acuña, M. H., Connerney, J. E. P., Wasilewski, P., Lin, R. P., Anderson, K. A., Carlson, C. W., et al. (1998). Magnetic field and plasma observations at Mars: Initial results of the Mars Global Surveyor mission. *Science*, 279(5357), 1676–1680. <https://doi.org/10.1126/science.279.5357.1676>
- Angelopoulos, V., Cruce, P., Drozdov, A., Grimes, E. W., Hatzigeorgiu, N., King, D. A., et al. (2019). The space physics environment data analysis system (SPEDAS). *Space Science Reviews*, 215(1), 9. <https://doi.org/10.1007/s11214-018-0576-4>
- Azari, A. R., Abrahams, E., Sapienza, F., Mitchell, D. L., Biersteker, J., Xu, S., et al. (2023). Magnetic field draping in induced magnetospheres: Evidence from the MAVEN mission to Mars. *Journal of Geophysical Research: Space Physics*, 128(11), e2023JA031546. <https://doi.org/10.1029/2023ja031546>

Acknowledgments

We acknowledge NASA and the MAVEN mission for support partially through grant NNH10CC04C to the University of Colorado and by subcontract to Space Sciences Laboratory, University of California, Berkeley. N.R. is supported by NASA under award number 80GSFC21M0002. JSH acknowledges the NASA Solar System Workings program for support through Grant 80NSSC20K0571.

- Bertucci, C., Duru, F., Edberg, N., Fraenz, M., Martinez, C., Szego, K., & Vaisberg, O. (2011). The induced magnetospheres of Mars, Venus, and Titan. *Space Science Reviews*, 162(1–4), 113–171. <https://doi.org/10.1007/s11214-011-9845-1>
- Brain, D. A., Bagenal, F., Acuña, M. H., & Connerney, J. E. P. (2003). Martian magnetic morphology: Contributions from the solar wind and crust. *Journal of Geophysical Research*, 108(A12), 1424. <https://doi.org/10.1029/2002JA009482>
- Brecht, S. H. (1997). Hybrid simulations of the magnetic topology of Mars. *Journal of Geophysical Research*, 102(A3), 4743–4750. <https://doi.org/10.1029/96JA03205>
- Breus, T. K., Krymskii, A. M., Lundin, R., Dubinin, E. M., Luhmann, J. G., Yeroshenko, Y. G., et al. (1991). The solar wind interaction with Mars: Consideration of Phobos 2 mission observations of an ion composition boundary on the dayside. *Journal of Geophysical Research*, 96(A7), 11165–11174. <https://doi.org/10.1029/91JA01131>
- Cairns, I. H., Fairfield, D. H., Anderson, R. R., Carlton, V. E. H., Paularena, K. I., & Lazarus, A. J. (1995). Unusual locations of Earth's bow shock on September 24–25, 1987: Mach number effects. *Journal of Geophysical Research*, 100(A1), 47–62. <https://doi.org/10.1029/94JA01978>
- Chai, L., Wan, W., Wei, Y., Zhang, T., Exner, W., Fraenz, M., et al. (2019). The induced global looping magnetic field on Mars. *The Astrophysical Journal*, 871(2), L27. <https://doi.org/10.3847/2041-8213/aaff6e>
- Cloutier, P. A., Law, C. C., Crider, D. H., Walker, P. W., Chen, Y., Acuña, M. H., et al. (1999). Venus-like interaction of the solar wind with Mars. *Geophysical Research Letters*, 26(17), 2685–2688. <https://doi.org/10.1029/1999GL900591>
- Connerney, J. E. P. (2017). MAVEN magnetometer (MAG) calibrated data bundle. *Planetary Data System*. <https://doi.org/10.17189/1414178>
- Connerney, J. E. P., Espley, J., Lawton, P., Murphy, S., Odom, J., Oliverson, R., & Sheppard, D. (2015). The MAVEN magnetic field investigation. *Space Science Reviews*, 195(1–4), 257–291. <https://doi.org/10.1007/s11214-015-0169-4>
- DiBraccio, G. A., Luhmann, J. G., Curry, S. M., Espley, J. R., Xu, S., Mitchell, D. L., et al. (2018). The twisted configuration of the Martian magnetotail: MAVEN observations. *Geophysical Research Letters*, 45(10), 4559–4568. <https://doi.org/10.1029/2018GL077251>
- DiBraccio, G. A., Romanelli, N., Bowers, C. F., Gruesbeck, J. R., Halekas, J. S., Ruhunusiri, S., et al. (2022). A statistical investigation of factors influencing the magnetotail twist at Mars. *Geophysical Research Letters*, 49(12), e2022GL098007. <https://doi.org/10.1029/2022GL098007>
- Dimmock, A. P., Osmane, A., Pulkkinen, T. I., & Nykyri, K. (2015). A statistical study of the dawn-dusk asymmetry of ion temperature anisotropy and mirror mode occurrence in the terrestrial dayside magnetosheath using THEMIS data. *Journal of Geophysical Research: Space Physics*, 120(7), 5489–5503. <https://doi.org/10.1002/2015JA021192>
- Dubinin, E., Fraenz, M., Pätzold, M., Tellmann, S., Modolo, R., DiBraccio, G., et al. (2023). Magnetic fields and plasma motions in a hybrid Martian magnetosphere. *Journal of Geophysical Research: Space Physics*, 128(1), e2022JA030575. <https://doi.org/10.1029/2022JA030575>
- Dubinin, E., Fränz, M., Woch, J., Roussos, E., Barabash, S., Lundin, R., et al. (2006). Plasma morphology at Mars. Aspera-3 observations. *Space Science Reviews*, 126(1–4), 209–238. <https://doi.org/10.1007/s11214-006-9039-4>
- Edberg, N. J. T., Brain, D. A., Lester, M., Cowley, S. W. H., Modolo, R., Fränz, M., & Barabash, S. (2009). Plasma boundary variability at Mars as observed by Mars Global Surveyor and Mars Express. *Annales Geophysicae*, 27(9), 3537–3550. <https://doi.org/10.5194/angeo-27-3537-2009>
- Edberg, N. J. T., Lester, M., Cowley, S. W. H., Brain, D. A., Fränz, M., & Barabash, S. (2010). Magnetosonic Mach number effect of the position of the bow shock at Mars in comparison to Venus. *Journal of Geophysical Research*, 115(A7), A07203. <https://doi.org/10.1029/2009JA014998>
- Edberg, N. J. T., Lester, M., Cowley, S. W. H., & Eriksson, A. I. (2008). Statistical analysis of the location of the Martian magnetic pileup boundary and bow shock and the influence of crustal magnetic fields. *Journal of Geophysical Research*, 113(A8), A08206. <https://doi.org/10.1029/2008JA013096>
- Fairfield, D. H. (1971). Average and unusual locations of the Earth's magnetopause and bow shock. *Journal of Geophysical Research*, 76(28), 6700–6716. <https://doi.org/10.1029/JA076i028p06700>
- Fairfield, D. H., Iver, H. C., Desch, M. D., Szabo, A., Lazarus, A. J., & Aellig, M. R. (2001). The location of low Mach number bow shocks at Earth. *Journal of Geophysical Research*, 106(A11), 25361–25376. <https://doi.org/10.1029/2000JA000252>
- Garnier, P., Jacquy, C., Gendre, X., Génot, V., Mazelle, C., Fang, X., et al. (2022). The drivers of the Martian bow shock location: A statistical analysis of Mars Atmosphere and Volatile Evolution N and Mars Express observations. *Journal of Geophysical Research: Space Physics*, 127(5), e2021JA030147. <https://doi.org/10.1029/2021JA030147>
- Garnier, P., Steckiewicz, M., Mazelle, C., Xu, S., Mitchell, D., Holmberg, M. K. G., et al. (2017). The Martian photoelectron boundary as seen by MAVEN. *Journal of Geophysical Research: Space Physics*, 122(10), 10472–10485. <https://doi.org/10.1002/2017JA024497>
- Gary, S. P., Fuselier, S. A., & Anderson, B. J. (1993). Ion anisotropy instabilities in the magnetosheath. *Journal of Geophysical Research*, 98(A2), 1481–1488. <https://doi.org/10.1029/92JA01844>
- Gary, S. P., McKean, M. E., Winske, D., Anderson, B. J., Denton, R. E., & Fuselier, S. A. (1994). The proton cyclotron instability and the anisotropy/beta inverse correlation. *Journal of Geophysical Research*, 99(A4), 5903–5914. <https://doi.org/10.1029/93JA03583>
- Gruesbeck, J. R., Espley, J. R., Connerney, J. E. P., DiBraccio, G. A., Soobiah, Y. I., Brain, D., et al. (2018). The three-dimensional bow shock of Mars as observed by MAVEN. *Journal of Geophysical Research: Space Physics*, 123(6), 4542–4555. <https://doi.org/10.1029/2018JA025366>
- Hajra, R., & Tsurutani, B. T. (2022). Near-Earth sub-Alfvénic solar winds: Interplanetary origins and geomagnetic impacts. *The Astrophysical Journal*, 926(2), 135. <https://doi.org/10.3847/1538-4357/ac4471>
- Halekas, J. S. (2017). MAVEN solar wind ion analyzer (SWIA) calibrated data bundle. *Planetary Data System*. <https://doi.org/10.17189/1414182>
- Halekas, J. S., Brain, D. A., Luhmann, J. G., DiBraccio, G. A., Ruhunusiri, S., Harada, Y., et al. (2017). Flows, fields, and forces in the Mars-solar wind interaction. *Journal of Geophysical Research: Space Physics*, 122(11), 11320–11341. <https://doi.org/10.1002/2017JA024772>
- Halekas, J. S., Luhmann, J. G., Dubinin, E., & Ma, Y. (2021). Induced magnetospheres. In *Magnetospheres in the Solar System* (pp. 391–406). American Geophysical Union (AGU).
- Halekas, J. S., McFadden, J. P., Brain, D. A., Luhmann, J. G., DiBraccio, G. A., Connerney, J. E. P., et al. (2018). Structure and variability of the Martian ion composition boundary layer. *Journal of Geophysical Research: Space Physics*, 123(10), 8439–8458. <https://doi.org/10.1029/2018JA025866>
- Halekas, J. S., Ruhunusiri, S., Harada, Y., Collinson, G., Mitchell, D. L., Mazelle, C., et al. (2017). Structure, dynamics, and seasonal variability of the Mars-solar wind interaction: MAVEN Solar Wind Ion Analyzer in-flight performance and science results. *Journal of Geophysical Research: Space Physics*, 122(1), 547–578. <https://doi.org/10.1002/2016JA023167>
- Halekas, J. S., Taylor, E. R., Dalton, G., Johnson, G., Curtis, D. W., McFadden, J. P., et al. (2015). The solar wind ion analyzer for MAVEN. *Space Science Reviews*, 195(1–4), 125–151. <https://doi.org/10.1007/s11214-013-0029-z>
- Hall, B. E. S., Sánchez-Cano, B., Wild, J. A., Lester, M., & Holmström, M. (2019). The Martian bow shock over solar cycle 23–24 as observed by the Mars Express mission. *Journal of Geophysical Research: Space Physics*, 124(6), 4761–4772. <https://doi.org/10.1029/2018JA026404>
- Hellinger, P., & Mangeney, A. (1999). Electromagnetic ion beam instabilities: Oblique pulsations. *Journal of Geophysical Research*, 104(A3), 4669–4680. <https://doi.org/10.1029/1998JA900157>
- Hill, P., Paschmann, G., Treumann, R. A., Baumjohann, W., Sckopke, N., & Lüher, H. (1995). Plasma and magnetic field behavior across the magnetosheath near local noon. *Journal of Geophysical Research*, 100(A6), 9575–9583. <https://doi.org/10.1029/94JA03194>

- Holmberg, M. K. G., André, N., Garnier, P., Modolo, R., Andersson, L., Halekas, J., et al. (2019). MAVEN and MEX multi-instrument study of the dayside of the Martian induced magnetospheric structure revealed by pressure analyses. *Journal of Geophysical Research: Space Physics*, *124*(11), 8564–8589. <https://doi.org/10.1029/2019JA026954>
- Jakosky, B. M., Grebowsky, J. M., Luhmann, J. G., Connerney, J., Eparvier, F., Ergun, R., et al. (2015). MAVEN observations of the response of Mars to an interplanetary coronal mass ejection. *Science*, *350*(6261), 0210. <https://doi.org/10.1126/science.aad0210>
- Janardhan, P. (2006). Enigmatic solar wind disappearance events – Do we understand them? *Journal of Astrophysics and Astronomy*, *27*(2), 201–207. <https://doi.org/10.1007/BF02702522>
- Janardhan, P., Tripathi, D., & Mason, H. E. (2008). The solar wind disappearance event of 11 May 1999: Source region evolution. *Astronomy and Astrophysics*, *488*(1), L1–L4. <https://doi.org/10.1051/0004-6361:200809667>
- Koval, A., Lepping, R. P., & Szabo, A. (2021). Wind magnetic field investigation (MFI) composite data [Dataset]. NASA Space Physics Data Facility. <https://doi.org/10.48322/AV38-WN55>
- Lavraud, B., & Borovsky, J. E. (2008). Altered solar wind-magnetosphere interaction at low Mach numbers: Coronal mass ejections. *Journal of Geophysical Research*, *113*(A9), A00B08. <https://doi.org/10.1029/2008JA013192>
- Law, C. C., & Cloutier, P. A. (1995). Observations of magnetic structure at the dayside ionopause of Venus. *Journal of Geophysical Research*, *100*(A12), 23973–23981. <https://doi.org/10.1029/95JA02756>
- Lazarus, A. J. (2000). The day the solar wind almost disappeared. *Science*, *287*(5461), 2172–2173. <https://doi.org/10.1126/science.287.5461.2172>
- Lepping, R. P., Acuña, M. H., Burlaga, L. F., Farrell, W. M., Slavin, J. A., Schatten, K. H., et al. (1995). The wind magnetic field investigation. *Space Science Reviews*, *71*(1–4), 207–229. <https://doi.org/10.1007/BF00751330>
- Luhmann, J. G. (1986). The solar wind interaction with Venus. *Space Science Reviews*, *44*(3–4), 241–306. <https://doi.org/10.1007/BF00200818>
- Luhmann, J. G., Dong, C. F., Ma, Y. J., Curry, S. M., Xu, S., Lee, C. O., et al. (2017). Martian magnetic storms. *Journal of Geophysical Research: Space Physics*, *122*(6), 6185–6209. <https://doi.org/10.1002/2016JA023513>
- Luhmann, J. G., & Russell, C. T. (1997). Venus: Magnetic field and magnetosphere. In *Encyclopedia of Planetary Science* (pp. 905–907). Springer. https://doi.org/10.1007/1-4020-4520-4_440
- Lundin, R., Barabash, S., Andersson, H., Holmström, M., Grigoriev, A., Yamauchi, M., et al. (2004). Solar wind-induced atmospheric erosion at Mars: First results from ASPERA-3 on Mars Express. *Science*, *305*(5692), 1933–1936. <https://doi.org/10.1126/science.1101860>
- Matsunaga, K., Seki, K., Brain, D. A., Hara, T., Masunaga, K., Mcfadden, J. P., et al. (2017). Statistical study of relations between the induced magnetosphere, ion composition, and pressure balance boundaries around Mars based on MAVEN observations. *Journal of Geophysical Research: Space Physics*, *122*(9), 9723–9737. <https://doi.org/10.1002/2017JA024217>
- Mazelle, C., Winterhalter, D., Sauer, K., Trotignon, J. G., Acuña, M. H., Baumgärtel, K., et al. (2004). Bow shock and upstream phenomena at Mars. *Space Science Reviews*, *111*(1), 115–181. <https://doi.org/10.1023/B:SPAC.0000032717.98679.d0>
- McComas, D. J., Spence, H. E., Russell, C. T., & Saunders, M. A. (1986). The average magnetic field draping and consistent plasma properties of the Venus magnetotail. *Journal of Geophysical Research*, *91*(A7), 7939–7953. <https://doi.org/10.1029/JA091iA07p07939>
- Mcfadden, J. P. (2023). MAVEN SupraThermal And Thermal Ion Composition (STATIC) calibrated data bundle. *Planetary Data System*. <https://doi.org/10.17189/1517741>
- McFadden, J. P., Kortmann, O., Curtis, D., Dalton, G., Johnson, G., Abiad, R., et al. (2015). MAVEN SupraThermal and Thermal Ion Composition (STATIC) Instrument. *Space Science Reviews*, *195*(1–4), 199–256. <https://doi.org/10.1007/s11214-015-0175-6>
- Mitchell, D. L. (2017). MAVEN Solar Wind Electron Analyzer (SWEA) calibrated data bundle. *Planetary Data System*. <https://doi.org/10.17189/1414181>
- Mitchell, D. L., Lin, R. P., Mazelle, C., Rème, H., Cloutier, P. A., Connerney, J. E. P., et al. (2001). Probing Mars' crustal magnetic field and ionosphere with the MGS Electron Reflectometer. *Journal of Geophysical Research*, *106*(E10), 23419–23428. <https://doi.org/10.1029/2000JE001435>
- Mitchell, D. L., Mazelle, C., Sauvaud, J. A., Thocaven, J. J., Rouzaud, J., Fedorov, A., et al. (2016). The MAVEN solar wind electron analyzer. *Space Science Reviews*, *200*(1–4), 495–528. <https://doi.org/10.1007/s11214-015-0232-1>
- Morschhauser, A., Lesur, V., & Grott, M. (2014). A spherical harmonic model of the lithospheric magnetic field of Mars. *Journal of Geophysical Research: Planets*, *119*(6), 1162–1188. <https://doi.org/10.1002/2013JE004555>
- Moses, S. L., Coroniti, F. V., & Scarf, F. L. (1988). Expectations for the microphysics of the Mars-solar wind interaction. *Geophysical Research Letters*, *15*(5), 429–432. <https://doi.org/10.1029/GL015i005p00429>
- Nagy, A. F., Winterhalter, D., Sauer, K., Cravens, T. E., Brecht, S., Mazelle, C., et al. (2004). The plasma environment of Mars. *Space Science Reviews*, *111*(1), 33–114. <https://doi.org/10.1023/B:SPAC.0000032718.47512.92>
- Ogilvie, K. W., Chornay, D. J., Fritzenreiter, R. J., Hunsaker, F., Keller, J., Lobell, J., et al. (1995). SWE, a comprehensive plasma instrument for the WIND spacecraft. *Space Science Reviews*, *71*(1), 55–77. <https://doi.org/10.1007/BF00751326>
- Ogilvie, K. W., Fritzenreiter, R. J., Lazarus, A. J., Kasper, J. C., & Stevens, M. (2021). Wind Solar Wind Experiment (SWE) 92-sec definitive solar wind proton data [Dataset]. NASA Space Physics Data Facility. <https://doi.org/10.48322/NASD-J276>
- Russell, C. T., & Zhang, T.-L. (1992). Unusually distant bow shock encounters at Venus. *Geophysical Research Letters*, *19*(8), 833–836. <https://doi.org/10.1029/92GL00634>
- Sauer, K., Bogdanov, A., & Baumgärtel, K. (1994). Evidence of an ion composition boundary (protonopause) in bi-ion fluid simulations of solar wind mass loading. *Geophysical Research Letters*, *21*(20), 2255–2258. <https://doi.org/10.1029/94GL01691>
- Skopke, N., Paschmann, G., Bame, S. J., Gosling, J. T., & Russell, C. T. (1983). Evolution of ion distributions across the nearly perpendicular bow shock: Specularly and non-specularly reflected-gyrating ions. *Journal of Geophysical Research*, *88*(A8), 6121–6136. <https://doi.org/10.1029/JA088iA08p06121>
- Skopke, N., Paschmann, G., Brinca, A. L., Carlson, C. W., & Lüher, H. (1990). Ion thermalization in quasi-perpendicular shocks involving reflected ions. *Journal of Geophysical Research*, *95*(A5), 6337–6352. <https://doi.org/10.1029/JA095iA05p06337>
- Soucek, J., Escoubet, C. P., & Grison, B. (2015). Magnetosheath plasma stability and ULF wave occurrence as a function of location in the magnetosheath and upstream bow shock parameters. *Journal of Geophysical Research: Space Physics*, *120*(4), 2838–2850. <https://doi.org/10.1002/2015JA021087>
- Steinolfson, R. S., & Cable, S. (1993). Venus bow shocks at unusually large distances from the planet. *Geophysical Research Letters*, *20*(8), 755–758. <https://doi.org/10.1029/93GL00839>
- Sui, H. Y., Wang, M., Lu, J. Y., Zhou, Y., & Wang, J. (2023). Interplanetary magnetic field effect on the location of the Martian bow shock: MAVEN observations. *The Astrophysical Journal*, *945*(2), 136. <https://doi.org/10.3847/1538-4357/acbd4c>
- Tatrallyay, M., Russell, C. T., Mihalov, J. D., & Barnes, A. (1983). Factors controlling the location of the Venus bow shock. *Journal of Geophysical Research*, *88*(A7), 5613–5621. <https://doi.org/10.1029/JA088iA07p05613>
- Thomsen, M. F., Gosling, J. T., Bame, S. J., & Mellott, M. M. (1985). Ion and electron heating at collisionless shocks near the critical Mach number. *Journal of Geophysical Research*, *90*(A1), 137–148. <https://doi.org/10.1029/JA090iA01p00137>

- Trotignon, J. G., Mazelle, C., Bertucci, C., & Acuña, M. H. (2006). Martian shock and magnetic pile-up boundary positions and shapes determined from the Phobos 2 and Mars Global Surveyor data sets. *Planetary and Space Science*, *54*(4), 357–369. <https://doi.org/10.1016/j.pss.2006.01.003>
- Verigin, M. I., Gringauz, K. I., Kotova, G. A., Remizov, A. P., Shutte, N. M., Rosenbauer, H., et al. (1993). The dependence of the Martian magnetopause and bow shock on solar wind ram pressure according to Phobos 2 TAUS ion spectrometer measurements. *Journal of Geophysical Research*, *98*(A2), 1303–1310. <https://doi.org/10.1029/92JA01666>
- Verigin, M. I., Slavin, J., Szabo, A., Kotova, G. A., Remizov, A., Rosenbauer, H., et al. (2004). Unusually distant bow shock encounters at Mars: Analysis of March 24, 1989 event. *Space Science Reviews*, *111*(1), 233–243. <https://doi.org/10.1023/B:SPAC.0000032713.86796.d1>
- Vignes, D., Acuña, M. H., Connerney, J. E. P., Crider, D. H., Rème, H., & Mazelle, C. (2002). Factors controlling the location of the bow shock at Mars. *Geophysical Research Letters*, *29*(9), 1328. <https://doi.org/10.1029/2001GL014513>
- Vignes, D., Mazelle, C., Rme, H., Acuña, M. H., Connerney, J. E. P., Lin, R. P., et al. (2000). The solar wind interaction with Mars: Locations and shapes of the bow shock and the magnetic pile-up boundary from the observations of the MAG/ER Experiment onboard Mars Global Surveyor. *Geophysical Research Letters*, *27*(1), 49–52. <https://doi.org/10.1029/1999GL010703>
- Wang, M., Xie, L., Lee, L. C., Xu, X. J., Kabin, K., Lu, J. Y., et al. (2020). A 3D parametric Martian bow shock model with the effects of Mach number, dynamic pressure, and the interplanetary magnetic field. *The Astrophysical Journal*, *903*(2), 125. <https://doi.org/10.3847/1538-4357/abbc04>
- Wei, Y., Fraenz, M., Dubinin, E., Coates, A. J., Zhang, T. L., Wan, W., et al. (2012). A teardrop-shaped ionosphere at Venus in tenuous solar wind. *Planetary and Space Science*, *73*(1), 254–261. <https://doi.org/10.1016/j.pss.2012.08.024>
- Xu, S., Liemohn, M. W., Dong, C., Mitchell, D. L., Bougher, S. W., & Ma, Y. (2016). Pressure and ion composition boundaries at Mars. *Journal of Geophysical Research: Space Physics*, *121*(7), 6417–6429. <https://doi.org/10.1002/2016JA022644>
- Xu, S., Mitchell, D. L., McFadden, J. P., Fowler, C. M., Hanley, K., Weber, T., et al. (2023). Photoelectron boundary: The top of the dayside ionosphere at Mars. *Journal of Geophysical Research: Space Physics*, *128*(5), e2023JA031353. <https://doi.org/10.1029/2023JA031353>
- Zhang, C., Rong, Z., Klinger, L., Nilsson, H., Shi, Z., He, F., et al. (2022). Three-dimensional configuration of induced magnetic fields around Mars. *Journal of Geophysical Research: Planets*, *127*(8), e2022JE007334. <https://doi.org/10.1029/2022JE007334>
- Zhang, T. L., Pope, S., Balikhin, M., Russell, C. T., Jian, L. K., Volwerk, M., et al. (2008). Venus Express observations of an atypically distant bow shock during the passage of an interplanetary coronal mass ejection. *Journal of Geophysical Research*, *113*(E9), E00B12. <https://doi.org/10.1029/2008JE003128>